Available online at www.sciencedirect.com

SciVerse ScienceDirect

Journal of the European Ceramic Society 32 (2012) 955–963

www.elsevier.com/locate/jeurceramsoc

Surface densification of porous ZrB_2–39 mol.% SiC ceramic composites by a laser process

Quentin Lonné, Nicolas Glandut*, Pierre Lefort

SPCTS, UMR 6638, CNRS, University of Limoges, Centre Européen de la Céramique, 12 Rue d'Atlantis, 87068 Limoges, France

Received 22 July 2011; received in revised form 11 October 2011; accepted 17 October 2011
Available online 25 November 2011

Abstract

40% porous composites ZrB_2–39 mol.% SiC were irradiated under a mobile laser beam, with a low power of 90 W, in a protective atmosphere of flowing argon. Quasi-full densification of the surface zone was obtained, with thicknesses of more than 20 μm. Temperature reached ca. 2500 °C and a fusible phase rich in SiC appeared, which partially dissolved the ZrB_2, favouring its sintering. The liquid phase filled the porosity present between the ZrB_2 grains, and migrated towards the surface and the bulk of the samples. After cooling, the liquid phase demixed, according to the ZrB_2–SiC phase diagram, and the phases ZrB_2 and SiC interweaved in a eutectic-like solid phase, co-existing with granular zones mainly composed of ZrB_2. Only few cracks were observed. Traces of free carbon were found at the surface, while oxygen never penetrated inside the samples, despite the presence of traces of this element in the surrounding atmosphere. These two last observations were explained by a thermodynamic study. The pellets so obtained could find applications in the fields of aerospace and of low-temperature protonic ceramic fuel cells.

Keywords: Laser; ZrB_2–SiC ceramic composites; Surface densification; Sintering

1. Introduction

Among ultra-high temperature ceramics (UHTCs), ZrB_2–SiC composites have been widely studied for the past decades because they offer a very interesting set of properties, such as a good resistance to oxidation and to thermal shocks, and a high thermal conductivity.[1–4] That is the reason why this kind of ceramics is one of the good candidates for high temperature applications, particularly in the aerospace field for hypersonic vehicles components like nose cones or wing leading edges.[5,6]

They also have a good electronic conductivity[7,8] and, as shown very recently, their oxidation provides a proton conductive surface glassy oxide, able to be used in low-temperature protonic ceramic fuel cells, LTPCFCs.[9]

Nevertheless, their densification remains difficult because of their high melting point[10–12] whereas a high density is required for many of their applications. For this reason, a laser treatment, which is a well-known promising process for densifying the surface of porous high temperature ceramics,[13–17] could bring significant progress in this field.

However, to the best of our knowledge, no study has been devoted to the laser densification of ZrB_2–SiC composites, but only to the laser densification of pure ZrB_2[14] or SiC,[18] or to the laser oxidation of ZrB_2–SiC composites.[13] Consequently, it seemed interesting to test the effect of a laser treatment on the surface of such ceramics, keeping in mind the potential application for LTPCFCs or aerospace field. It was the aim of the present work.

2. Experimental

2.1. Raw materials and apparatus

ZrB_2–SiC composites were obtained from ZrB_2 powder (Grade B, +97% pure) and α-SiC powder (Grade UF-25, +98% pure) purchased from H.C. Starck, USA. Table 1 gives the impurities of the powders, where oxygen appears to be the main one, with contents of 1.50 and 1.81 wt.% for ZrB_2 and SiC, respectively.

Fig. 1a shows that the SiC powder was composed of 5–10 μm large aggregates (sometimes even bigger) of submicronic grains.

---

* Corresponding author. Tel.: +33 5 55 45 75 54; fax: +33 5 87 50 23 07.
E-mail address: nicolas.glandut@unilim.fr (N. Glandut).

0955-2219/$ – see front matter © 2011 Elsevier Ltd. All rights reserved.
doi:10.1016/j.jeurceramsoc.2011.10.027

Table 1
Impurities of the starting powders.

Powder	Main impurities	
	Element	Content (wt.%)
ZrB_2	O	1.50
	N	0.25
	C	0.2
	Hf	0.2
	Fe	0.1
α-SiC	O	1.81
	Fe	0.04
	Al	0.03
	Ca	<0.01

A grain size analysis, carried out with a CILAS 1064 granulometer, gives a quasi-monomodal grain size distribution, ca. 0.5 μm.

ZrB_2 powder was composed of angular grains of 3–5 μm, accompanied of fine particles, that is the morphology of a crushed powder (Fig. 1b). Its grain size distribution, obtained as previously, is trimodal (ca. 0.9, 3.4, and 9 μm).

Pre-sintering (detailed below) was achieved in a furnace equipped with a graphite resistor (Nabertherm GmbH, Germany), and the final laser surface treatment was performed with a continuous wave ytterbium fibre laser (IPG, Oxford, MA, USA, model LCF100), as previously described in Ref. 15 (TEM_{00}, wavelength 1072 ± 10 nm, maximum power 100 W, spot diameter variable from 5 to 1 mm). A high-resolution motorized *X–Y* table, combined with an axes controller (Newport, CA, USA; models M-ILS100CC and ESP 300), allowed to treat a surface area of 6 mm × 6 mm, with different possible rates from 1 to 10 mm s^{-1}. The laser pattern is described in detail in Fig. 2. All the laser treatments were performed in a homemade cell, under flowing argon (Air Liquide, France, Grade Alphagaz 1, containing as main impurities $H_2O \leq 3$ ppm, and $O_2 \leq 2$ ppm), with a flow rate of ca. 2.8×10^{-4} m^3 s^{-1}, in order to avoid the oxidation of the samples.

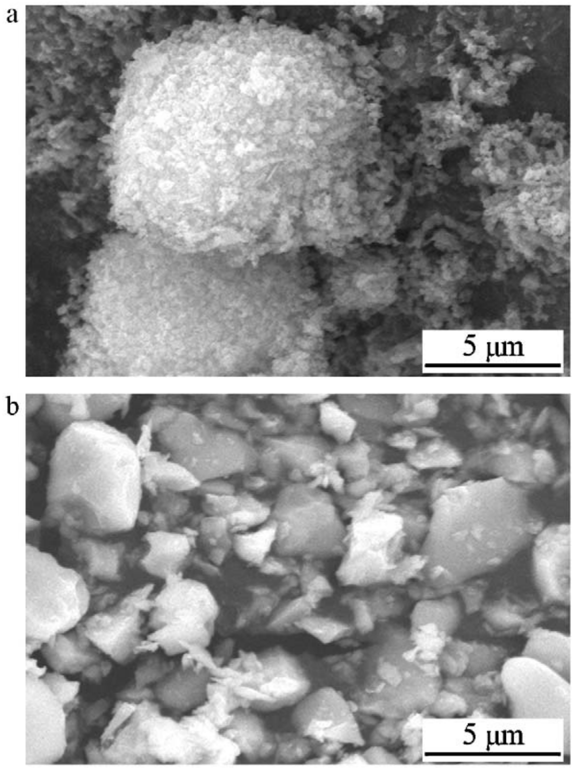

Fig. 1. SEM images of the starting powders: (a) SiC, and (b) ZrB_2.

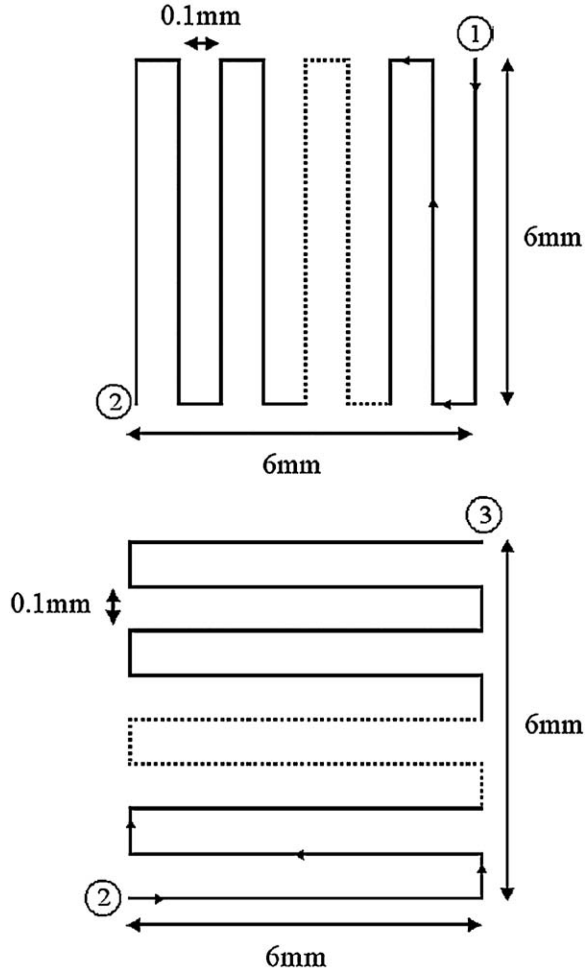

Fig. 2. Laser pattern on the surface of the composites. First, path 1 → 2 is realized and then, path 2 → 3 immediately overlaps path 1 → 2. The complete path 1 → 3 constitutes one cycle.

Microscopic observations were carried out using a scanning electron microscope (SEM Philips XL30) with in situ EDS (Oxford Instruments-INCA, UK). XRD was performed with a Siemens D5000 diffractometer, with a Cu anticathode and a back monochromator, working between 20° and 50° with a step of 0.02° and a 1.4 s exposure time. The X-ray patterns were indexed with a DIFFRAC+ EVA software (Bruker AXS) containing the JCPDS files database.

2.2. Sintering and characterization of the sintered samples

The powders were ultrasonically mixed during 5 min, in ligroin. Their relative contents were 18.5 wt.% of SiC and 81.5 wt.% of ZrB_2, i.e. 39 mol.% of SiC and 61 mol.% of ZrB_2.

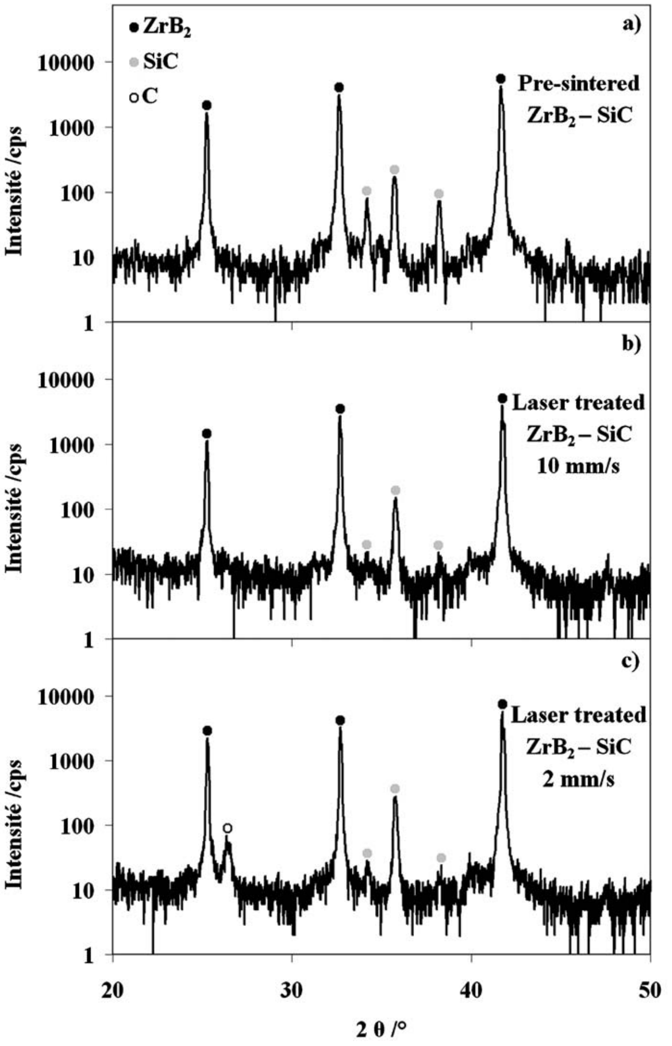

Fig. 3. XRD patterns of (a) the pre-sintered sample, (b) a sample irradiated at 10 mm s^{-1} (twice), (c) a sample irradiated at 2 mm s^{-1}. The logarithmic scale highlights the peak of free carbon.

The powders were pelletized by uniaxial cold pressing of 1.15 g of mixture in a 10-mm diameter die, under 30 MPa, without any binder or additive.

Sintering was achieved under argon (see quality above), with a 2.5-h dwell at 1700 °C, and heating and cooling rates of 10 °C min^{-1}.

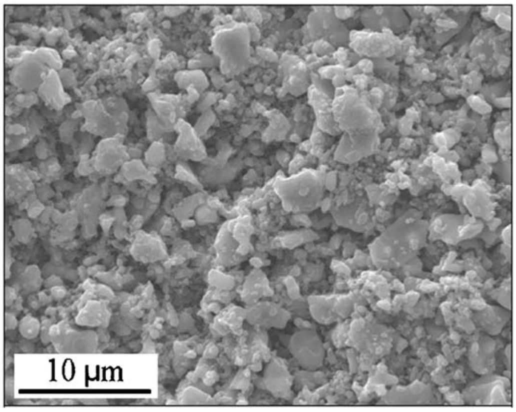

Fig. 4. SEM observation of a pre-sintered sample, representative of surface and bulk.

The pre-sintered pellets (9.7 mm in diameter, 3 mm thick) presented a high porosity, of about 40%. This was determined by weighting and measuring the samples, and compared to the theoretical density of the mixture, supposed to have not reacted quantitatively, as confirmed by the XRD analysis of Fig. 3a. They were first polished up to R_a of ca. 30 μm, then ultrasonically cleaned in acetone, and finally dried in air at 80 °C for 12 h. Fig. 4 provides an SEM micrograph representative of both the surface and the bulk of the pre-sintered pellets before laser irradiation. Despite the large difference in grain sizes and densities (3.16 g cm^{-3} for SiC and 6.09 g cm^{-3} for ZrB_2), the two powders have been mixed well, insofar as an homogeneous distribution of the big grains of ZrB_2 and of the smaller grains of SiC is observed. It can also be noticed that the grain morphologies changed only slightly, which confirms that the sintering was limited, but the strengthening obtained was sufficient for making the pellets impossible to break manually. Densification could have been easily improved using more drastic sintering conditions, but this seemed not useful for three reasons:

(i) The final laser treatment is easier and needs lower power densities for melting the surface when the samples are poorly densified. Indeed, because of the high thermal conductivities of the materials, the heat losses by thermal transfers towards the bulk of the samples are less intense in low-density pieces. Actually, the thermal conductivity of ZrB_2 is of 56 W m^{-1} K^{-1} at room temperature, increasing up to 67 W m^{-1} K^{-1} at 1675 K[7]; it reaches 125 W m^{-1} K^{-1} for sintered SiC, and even 490 W m^{-1} K^{-1} for 6H single-crystals[7];
(ii) Many high-temperature applications, particularly in the aerospace field, only need a densified surface (that will be obtained by laser treatment) to promote a good oxidation resistance, and can have a porous bulk as far as they keep sufficient mechanical properties;
(iii) The application to LTPCFCs implies that the gases could penetrate inside the cell, which requires a high porosity of the solid.

For the surface and for the bulk, XRD identified no extra phase other than SiC and ZrB_2, and EDS only detected elements Zr, Si, C, and B, which showed that there was no quantitative reaction between these phases or with oxygen.

2.3. Laser treatment

Surface densification was achieved with a laser power of 90 W and a spot diameter of 1 mm corresponding to a power density of 11.5 kW cm^{-2}. The treatment comprised either one pass at 2 mm s^{-1} or at 3 mm s^{-1}, or two successive passes at the same place at 10 mm s^{-1} (noted 10 mm s^{-1} (twice), below), as described in Fig. 2. This process was determined empirically, by considering that:

(i) Power densities lower than 11.5 kW cm^{-2} did not allow densifying completely and homogeneously the surface;
(ii) Beam rates below 2 mm s^{-1} gave very inhomogeneous surfaces with severe cracks;
(iii) For rates of 10 mm s^{-1} or more, densification remained insufficient after one pass, and it required a second cycle overlapping the first one.

The total, incident energy received by the sample could be estimated approximately at mean values going from 13.4 kJ for a laser scanning of 10 mm s^{-1} (twice), to 22.3 kJ and 33.5 kJ for the laser rates of 3 mm s^{-1} and 2 mm s^{-1}, respectively.

3. Results

The laser treatment induced noticeable changes in the microstructure of the pre-sintered samples, accompanying the densification of their surface. The morphology and the composition of the surface were modified, as well as the inner heat-affected zone (HAZ) just underneath the surface.

3.1. *Surface of the laser treated composites*

XRD identified only ZrB_2 and SiC diffraction peaks on the surfaces of the samples treated at 10 mm s^{-1} (twice) (Fig. 3b), whereas a peak corresponding to free carbon appeared in the patterns for the samples treated at 2 and 3 mm s^{-1} (e.g. in Fig. 3c for a laser rate of 2 mm s^{-1}). Note here that no carbon was initially detected, in the starting powders and in the pre-sintered pellets (Fig. 3a).

For the three laser rates, SEM observations of the surface always showed two kinds of regions with different morphologies, called "region 1" and "region 2". Figs. 5 and 6 present these two regions on the surface of a sample treated at a laser rate of 3 mm s^{-1}:

- For region 1, Fig. 5a presents the features of a lamellar eutectic, with some small pores. This morphology is characteristic, and evidences that the samples surface melted under the laser beam. The SEM micrograph of the lamellae is magnified in Fig. 5b, in backscattered electron (BSE) mode. The location of the two phases can be defined, the brighter containing the heavier element (Zr), hence attributed to ZrB_2 areas, and the darker corresponding to the lighter element (Si), i.e. to the SiC phase.
- Region 2, shown in Fig. 6a was a granular zone, whose grain size, close to that of Fig. 1b, indicated that it was composed of the diboride ZrB_2 grains. Fig. 6b shows that these grains were sintered and covered with small platelets, between 500 nm and 1 μm large. Their surfaces seemed attacked (compare with Fig. 1b). In the hollows located at the junction of three grains, the BSE observation of Fig. 6c reveals the presence of another phase, appearing in dark, hence probably rich in silicon, while the ZrB_2 grains are bright, and linked together by necks.

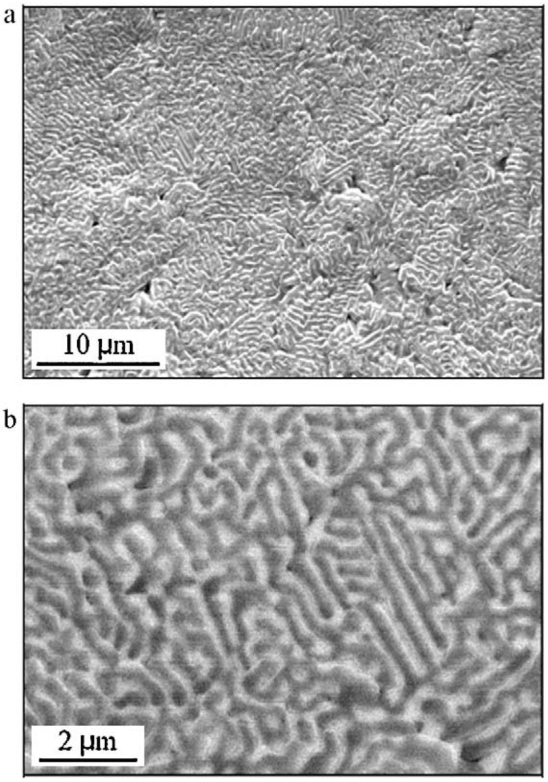

Fig. 5. (a) Surface observation of a eutectic-type region after treatment at 3 mm s^{-1}; (b) magnification of (a), in BSE mode.

Some superficial cracks were observed, as reported in Fig. 7a (e.g., on a sample treated at 10 mm s^{-1}). They were likely due to thermal shock during heating or residual stresses during cooling,[13,15,19,20] but they were sometimes healed as seen in Fig. 7b (e.g., on a sample treated at 2 mm s^{-1}). Actually, a kind of continuous thin film covers the whole sample surface.

EDS detected the only elements Zr, B, Si and C, and never oxygen (Fig. 8), in spite of the presence of traces of this last element in the starting powders and in the argon used. Quantitative analysis could only be performed on the heaviest elements. They showed that the [Si]/[Zr] ratio increased on the surface of the samples, in the eutectic-type zones, when the laser beam rate decreased, i.e. for the highest transmitted energies. Table 2 provides the content of the elements Zr and Si in the samples before laser treatment, and for the three scanning rates, considering the two types of regions. The original atomic ratio [Si]/[Zr] found, 0.59, is close to the expected one on the basis of the composition of the initial mixture, i.e. 0.64. After the laser treatments, the eutectic-type regions have majority contents in silicon (from 55 at.% for the samples treated at 10 mm s^{-1} (twice) to 77 at.% for rates of 2 mm s^{-1}). At the opposite, the granular regions are richer in zirconium (up to 86 at.% after an irradiation at 10 mm s^{-1} (twice)) except for the slower rate of 2 mm s^{-1}, where the content of zirconium was of 58 at.% only.

3.2. *Cross-sections of the laser treated composites*

In the cross-sections, a dense layer was observed at the top of the composites, with mean thicknesses of 24, 25 and 39 ± 2 μm,

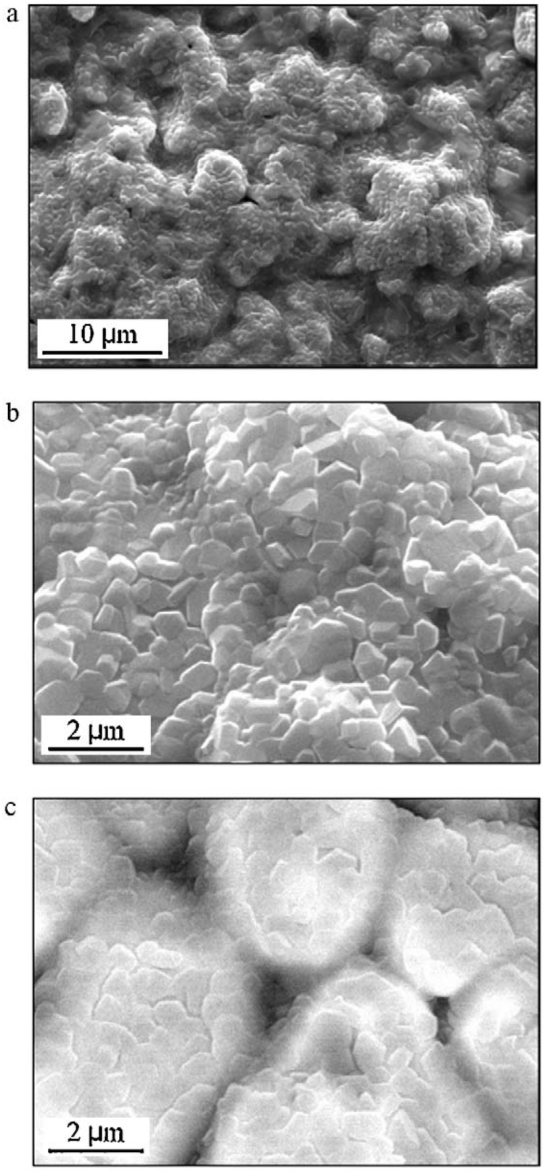

Fig. 6. (a) Surface observation of a granular region after treatment at 3 mm s^{-1}; (b) magnification of (a); (c) same view than (b), but in BSE mode.

for the treatments at 10 (twice), 3 and 2 mm s^{-1}, respectively. Fig. 9a and b shows that this layer presented the features of a melted zone. It was homogeneous, of variable thickness, with only some small pores, the biggest reaching 5 µm in diameter. The interface melted/not melted composite was plane, and below, the microstructure of the material was not affected (compare with Fig. 4). The dense layer was composed of a mix of the granular and eutectic microstructures, the eutectic one being particularly present for the most energetic treatment (laser rate of 2 mm s^{-1}) as seen in Fig. 9c, while the granular microstructure was majority for the laser rate of 10 mm s^{-1} (twice) (Fig. 9d). The eutectic microstructure was found at the surface and below, at the interface between the HAZ and the non-HAZ zones, as seen at the bottom of Fig. 9c, and magnified in Fig. 9e. At the top of the HAZ, there was a thin film covering the surface, mainly visible in the micrograph of the samples treated at 2 mm s^{-1}, as in Fig. 9f, where its thickness was about 1–2 µm.

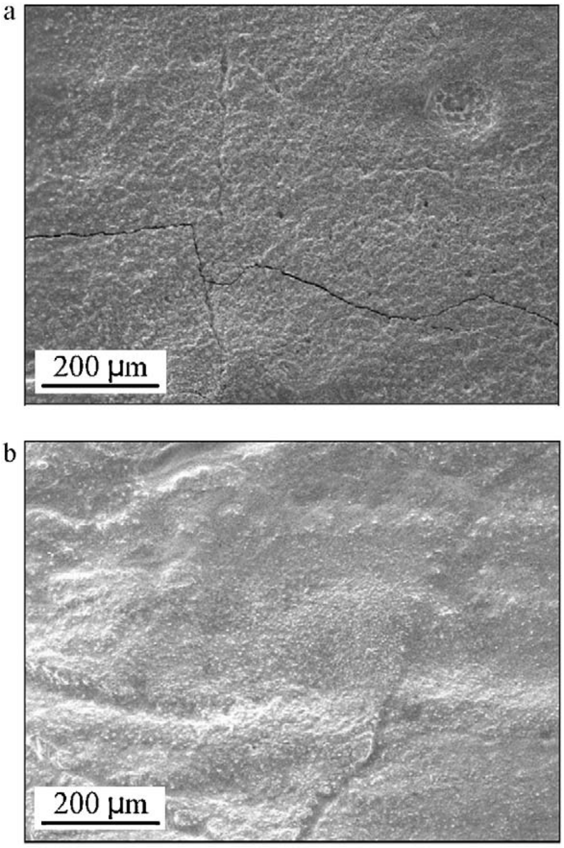

Fig. 7. Top views. (a) Crack on a sample treated at 10 mm s^{-1} (twice). (b) Laser-healed crack on a sample treated at 2 mm s^{-1}.

Mappings of polished cross section of samples irradiated at the different laser rates were performed for the two elements Zr and Si, boron and carbon analyses being not reliable. The BSE micrograph of a sample treated at 2 mm s^{-1} is given in Fig. 10a (this rate was chosen because the thin surface film was the most visible at this rate, but it is representative of all the samples). On the Zr X-ray map of Fig. 10b, the HAZ appears brighter than the non-affected composite below, which means that it was richer in zirconium. Correlatively this zone was Si-depleted as it can

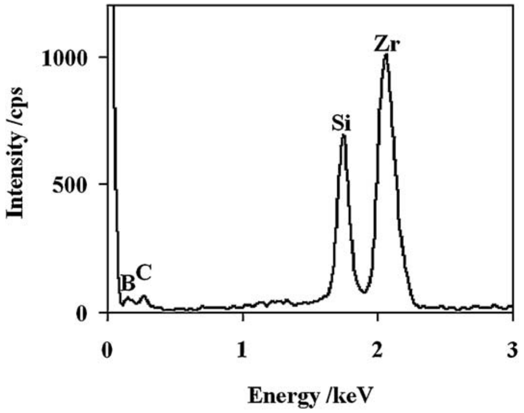

Fig. 8. EDS spectrum of the surface of a sample treated at 10 mm s^{-1}.

Table 2
Zr and Si surface contents, as determined by EDS, for the three scanning rates, and for the two types of regions.

Scanning rate ($mm\,s^{-1}$)	Region	Element	Content (at.%)	Si/Zr
0 (base sample)	Original surface	Zr	63	0.59
		Si	37	
2	Granular	Zr	58	0.72
		Si	42	
	Eutectic-type	Zr	23	3.35
		Si	77	
3	Granular	Zr	70	0.43
		Si	30	
	Eutectic-type	Zr	38	1.63
		Si	62	
10 (twice)	Granular	Zr	86	0.16
		Si	14	
	Eutectic-type	Zr	45	1.22
		Si	55	

be observed in the Si X-ray map of Fig. 10c that reveals also that the thin superficial film contained mainly silicon and only little zirconium. These maps show also that the initial mixture was not perfect, since several areas, of ca. 10–15 μm, in the sintered part of the samples, contain only the carbide SiC. At the opposite, it is worth noticing that the densified crust is much more homogeneous.

4. Discussion

The laser treatment of 40%-porous composites ZrB_2–39 mol.% SiC densified quasi-fully a surface zone of 0.36 cm^2 in area, of more than 20 μm thick, for durations of around 1 min, with only some cracks. This result was obtained via a liquid phase sintering process, thanks to a mechanism explained below.

4.1. Sintering mechanism

In order to propose a sintering mechanism, the following features must be first taken into account:

(i) The melting concerned a large part of the constituents, which formed the eutectic-type regions, after cooling;
(ii) The original grains of SiC entirely disappeared, in the HAZ;
(iii) The original grains of ZrB_2 almost kept their initial morphology, showing that they have only be little affected during the sintering. Nevertheless, the necks well visible in the BSE image of Fig. 6c, evidence that ZrB_2 participated to the sintering process, as well as the presence of zirconium inside the eutectic-type regions;
(iv) No extra phase was detected after cooling, except the components ZrB_2 and SiC, and sometimes free carbon as seen in Fig. 3c. However, the presence of eutectic-type regions containing both zirconium and silicon proves that a liquid phase containing ZrB_2 and SiC existed during the melting under the laser beam.

These elements led us to propose the following process, for justifying the remarkable surface densification observed.

Under the laser beam, temperature grew very quickly with a rate estimated between 5000 and 25,000 $°C\,s^{-1}$ according to the laser rate, and considering that temperature reached around 2500 °C. Indeed, the temperature remained likely below 2760 °C where SiC decomposes at atmospheric pressure,[12,21] since SiC was always present after cooling. But temperature certainly exceeded 2270 °C, which is the eutectic temperature of formation of the liquid phase in the pseudo-binary system ZrB_2–SiC[12] reported in Fig. 11.

Under these conditions, at the contacts between the grains of ZrB_2 and of SiC, a liquid phase rich in SiC must form very quickly. It rapidly dissolved entirely the small grains of SiC, and partially those of ZrB_2. Near the surface of ZrB_2, this liquid phase acted likely as a secondary phase in a liquid phase sintering, which explains the formation of necks between the diboride grains, seen in Fig. 6c. Logically, this liquid phase attacked preferentially the diboride at the grain boundaries of the original ZrB_2 grains, giving the facies seen also in Fig. 6c. During this process of densification of ZrB_2, the liquid phase rich in SiC, was expelled towards the hollows between the grains of ZrB_2, towards the surface of the sample, where it could gather in pools, and towards the interface between HAZ and non-HAZ. Its presence at the surface was the most noticeable for the highest temperatures (the lowest laser rates), which explains that the granular surface zones seemed apparently less rich in ZrB_2 than the others, in Table 2.

During cooling, the demixing of the liquid phase occurred, since the mutual solubility of the components ZrB_2 and SiC is negligible.[12,22,23] This gave the eutectic-type morphology observed at the surface (Fig. 5), inside the HAZ and also at the interface HAZ/non-HAZ (Fig. 9e).

This mechanism explains well the good densification of the crust of the samples, mainly due to the sintering of ZrB_2.

4.2. Surface reactions

Since a SiC-rich phase migrates towards the surface, and considering that SiC reacts easily with oxygen,[24] one could expect oxygen to be found at the surface of the samples after the laser treatment. Indeed, traces of oxygen are present in the argon ($P_{O_2} \approx 0.2$ Pa) and air leaks inside the treatment cell are possible. Nevertheless, oxygen was never detected in the samples, while traces of carbon were (see e.g. Fig. 3c). In a first approach, a thermodynamic study was carried out in order to understand this behaviour.

A volatility diagram of the SiC/O_2 system has been calculated and plotted in Fig. 12 for a temperature of 2700 K (2427 °C) and for low oxygen partial pressures, on the basis of thermodynamical tables.[25] More details about building this kind of diagrams can be found in the literature.[22,24,26,27] The condensed phase SiC is thermodynamically stable inside the zones delimited by the solid lines, function of the oxygen partial pressure,

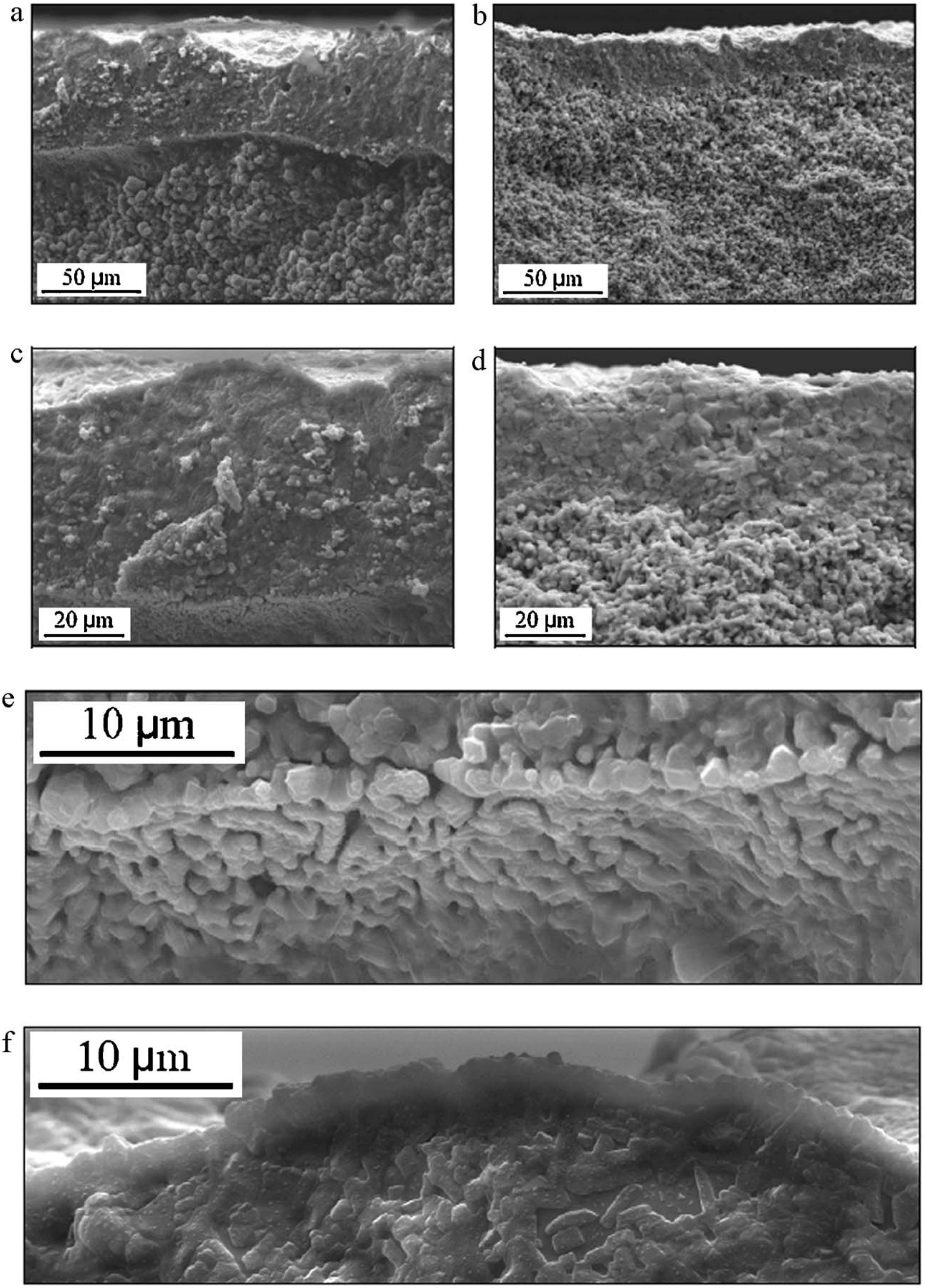

Fig. 9. SEM observations of fractured cross-sections. (a) and (b) General views of samples treated at 2 and 10 mm s^{-1} (twice), respectively. (c) and (d) Upper parts of (a) and (b), respectively. (e) Detail of the eutectic microstructure at the interface between the HAZ and the non-HAZ zones of the sample treated at 2 mm s^{-1}. (f) Detail of the thin surface layer of the sample treated at 2 mm s^{-1}.

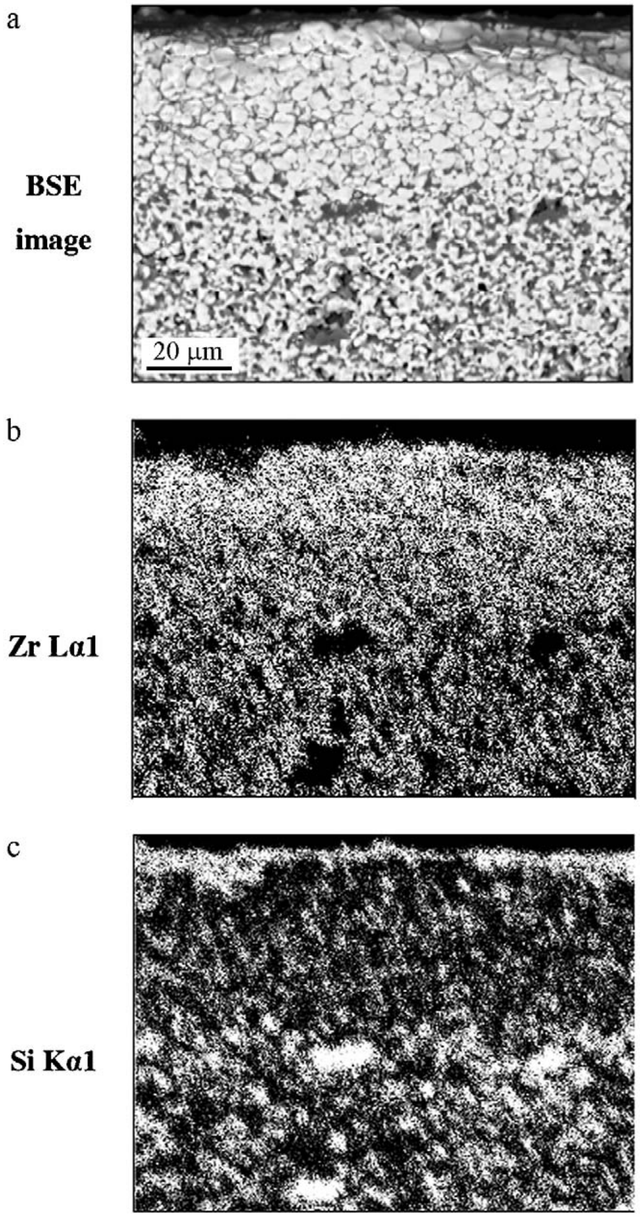

Fig. 10. (a)–(c) BSE image, Zr, and Si X-ray maps, respectively, of the polished cross section of a sample treated at 2 mm s^{-1}.

P_{O_2}. For instance, for $P_{O_2} = 10^{-7}$ Pa (log $P_{O_2} = -7$), the condensed stable phase SiC is in equilibrium with the gaseous phase SiO (silicon monoxide) with a high partial pressure ($P_{SiO} = 10^{4.91}$ Pa = 8.13 10^4 Pa). It is worth noticing that, for gaseous species, the boundaries delimit only predominance domains. For that, the separation between $Si_{(g)}$ and $SiO_{(g)}$ is plotted in dotted line (e.g. for $P_{O_2} = 10^{-7}$ Pa, again, the gaseous species that evolves from $SiC_{(s)}$ is $SiO_{(g)}$ alone, but $SiO_{(g)}$ partially converts into $Si_{(g)}$ even if the thermodynamical calculations indicate that $SiO_{(g)}$ is the predominant species).

Now, let us assume that the oxygen partial pressure in the inlet gas was around 0.2 Pa, i.e. according to the gas characteristics given by the supplier. It can react with SiC, giving $SiO_{(g)}$, the effect of which should be to reduce the partial pressure of oxygen to a very low value, calculated as equal to $10^{-18.22}$ Pa, on the basis of Eq. (1)

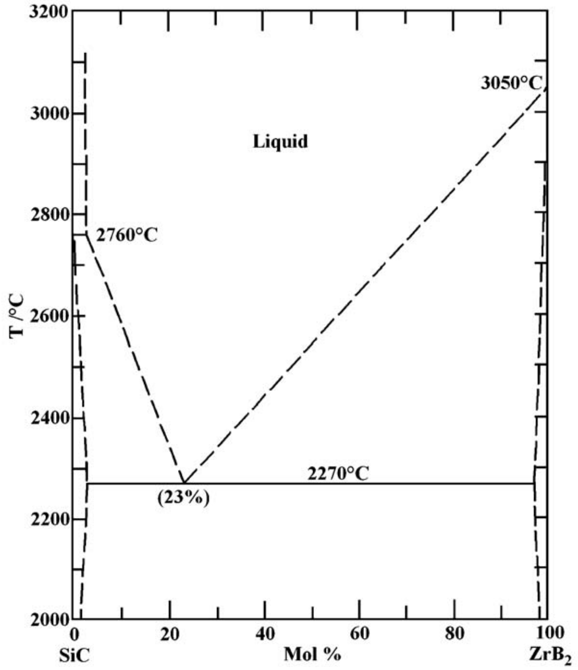

Fig. 11. Pseudo-binary phase diagram ZrB$_2$–SiC.
Source: Ref. [12].

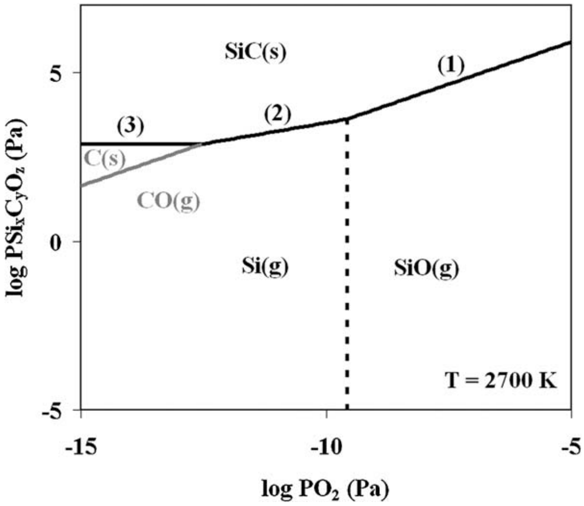

Fig. 12. Volatility diagram of the system SiC/O$_2$ at 2700 K. Equilibria (1)–(3): see Section 4.2.

$$SiC(s) + O_2 = SiO(g) + CO(g) \qquad (1)$$

and considering the corresponding equilibrium constant $K_1 = 10^{11.823}$ (pressure of reference = 1 bar).

But, for oxygen partial pressures lower than $10^{-9.58}$ Pa, the oxidation of SiC becomes

$$SiC(s) + 1/2O_2 = Si(g) + CO(g) \qquad (2)$$

and, when the oxygen partial pressure falls at $10^{-12.52}$ Pa, the carbide decomposes, giving free carbon, according to Eq. (3)

$$SiC(s) \rightarrow Si(g) + C(s) \qquad (3)$$

This explains why oxygen never penetrated inside the sample, since it formed the gaseous phase SiO, which departs with the argon flow. This also explains the presence of free carbon on the top surface of the samples. This effect was the most noticeable when the temperature was the highest. For instance, the equilibrium $Si_{(g)}$ partial pressure increases with temperature, passing from $10^{2.89}$ Pa at 2427 °C to $10^{3.87}$ Pa at 2727 °C. Actually, carbon has been detected by XRD on the samples treated at a laser rate of 2 and 3 $mm\,s^{-1}$, i.e. in the conditions where the temperatures were the highest, but it was also probably present, but weakly, at the rate of 10 $mm\,s^{-1}$ (twice). This free carbon might contribute to the healing of cracks seen in Fig. 7b, but it is also possible that $Si_{(g)}$, emanating from the zone just under the laser beam (through Eqs. (2) and (3)), condensates on the cracks, in colder zones, slightly distant from the laser beam. Only a fine surface analysis could clarify this point.

5. Conclusion

This work confirms the feasibility of the laser surface densification of porous ZrB_2–SiC pieces. Even using a lab-bench laser, with a relatively low power of 90 W, a dense crust more than 20-μm thick was obtained in less than 2 min on a surface area of 0.36 cm^2, despite the high-refractory properties of this composite.

This opens the field of the two following applications:

(i) The perimeter densification, or airtighting, of this kind of porous ceramic could be useful in aerospace, because it could permit the lightening of certain pieces. Indeed, a dense crust would allow high-temperature and surface-limited oxidation, avoiding oxidation inside the porous bulk, by forming a borosilicate glass;

(ii) The laser process described in the present paper could be used under oxidizing atmosphere on porous ZrB_2–SiC, in order to fabricate half low-temperature protonic ceramic fuel cells, LTPCFCs. This kind of new half fuel cell has been very recently introduced, and consists in a dense, crack-free, proton conducting, SiO_2-rich glass covering a porous ZrB_2–SiC gas diffusion electrode.[9]

Acknowledgement

We gratefully acknowledge the Région Limousin for Q.L.'s Ph.D. scholarship.

References

1. Zimmermann JW, Hilmas GE, Fahrenholtz WG. Thermal shock resistance of ZrB_2 and ZrB_2–30% SiC. *Mater Chem Phys* 2008;**112**(1):140–5.
2. Hu P, Guolin W, Wang Z. Oxidation mechanism and resistance of ZrB_2–SiC composites. *Corros Sci* 2009;**51**(11):2724–32.
3. Han J, Hu P, Zhang X, Meng S, Han W. Oxidation-resistant ZrB_2–SiC composites at 2200 °C. *Compos Sci Technol* 2008;**68**(3–4):799–806.
4. Rezaie A, Fahrenholtz WG, Hilmas GE. Evolution of structure during the oxidation of zirconium diboride–silicon carbide in air up to 1500 °C. *J Eur Ceram Soc* 2007;**27**(6):2495–501.
5. Wuchina E, Opila E, Opeka M, Fahrenholtz WG, Talmy I. UHTCs: ultra-high temperature ceramic materials for extreme environment applications. *Electrochem Soc* 2007;**16**(4):30–6.
6. Opeka MM, Talmy IG, Zaykoski JA. Oxidation-based materials selection for 2000 °C + hypersonic aerosurfaces: theoretical considerations and historical experience. *J Mater Sci* 2004;**39**(19):5887–904.
7. Zimmermann JW, Hilmas GE, Fahrenholtz WG, Dinwiddie RB, Porter WD, Wang H. Thermophysical properties of ZrB_2 and ZrB_2–SiC ceramics. *J Am Ceram Soc* 2008;**91**(5):1405–11.
8. Karlsdottir SN, Halloran JW. Rapid oxidation characterization of ultra-high temperature ceramics. *J Am Ceram Soc* 2007;**90**(10):3233–8.
9. Lonné Q, Glandut N, Labbe J-C, Lefort P. Fabrication and characterization of ZrB2–SiC ceramic electrodes coated with a proton conducting SiO_2-rich glass layer. *Electrochim Acta* 2011;**56**(20):7212–9.
10. Zhang SC, Hilmas GE, Fahrenholtz WG. Pressureless sintering of ZrB_2–SiC ceramics. *J Am Ceram Soc* 2008;**91**(1):26–32.
11. Rezaie A, Fahrenholtz WG, Hilmas GE. Effect of hot pressing time and temperature on the microstructure and mechanical properties of ZrB_2–SiC. *J Mater Sci* 2007;**42**(8):2735–44.
12. McHale AE, McMurdie HF, Ondik HM, Clevinger MA, Hill KM, Green T, et al. Phase equilibria diagrams. *Borides, carbides and nitrides*, vol. X, 2nd ed. Columbus, OH: The American Ceramic Society; 1994. p. 8.
13. Jayaseelan DD, Jackson H, Eakins E, Brown P, Lee WE. Laser modified microstructures in ZrB_2, ZrB_2/SiC and ZrC. *J Eur Ceram Soc* 2010;**30**(2):2279–88.
14. Sun C-N, Gupta MC. Laser sintering of ZrB_2. *J Am Ceram Soc* 2008;**91**(5):1729–31.
15. Bacciochini A, Glandut N, Lefort P. Surface densification of porous ZrC by a laser process. *J Eur Ceram Soc* 2009;**29**(8):1507–11.
16. White RM, Kunkle JM, Polotai AV, Dickey EC. Microstructure and hardness scaling in laser-processed B_4C–TiB_2 eutectic ceramics. *J Eur Ceram Soc* 2010;**31**(7):1227–32.
17. Polotai AV, Foreman JF, Dickey EC. Laser surface processing of B_4C–TiB_2 eutectic. *Int J Appl Ceram Technol* 2008;**5**(6):610–7.
18. Gupta S, Molian P. Design of laser micromachined single crystal 6H-SiC diaphragms for high-temperature micro-electro-mechanical-system pressure sensors. *Mater Des* 2011;**32**(1):127–32.
19. Triantafyllidis D, Li L, Stott FH. Crack-free densification of ceramics by laser surface treatment. *Surf Coat Technol* 2006;**201**(6):3163–73.
20. Gusarov AV, Pavlov M, Smurov I. Residual stresses at laser surface remelting and additive manufacturing. *Phys Procedia* 2011;**12**(1):248–54.
21. Sciti D, Bellosi A. Laser-induced surface drilling of silicon carbide. *Appl Surf Sci* 2001;**180**(1–2):92–101.
22. Fahrenholtz WG. Thermodynamic analysis of ZrB_2–SiC oxidation: formation of a SiC-depleted region. *J Am Ceram Soc* 2007;**90**(1):143–8.
23. Liang J, Wang Y, Meng S. Interface and defect characterization in hot-pressed ZrB_2–SiC ceramics. *Int J Refract Met Hard Mater* 2011;**29**(3): 341–3.
24. Heuer AH, Lou VLK. Volatility diagrams for silica, silicon nitride silicon carbide and their application to high-temperature decomposition and oxidation. *J Am Ceram Soc* 1990;**73**(10):2789–803.
25. Chase Jr MW. *NIST-JANAF thermochemical tables*. 4th ed. New York: American Institute of Physics and American Chemical Society; 1998.
26. Lefort P, Tetard D, Tristant P. Formation of aluminium carbide by carbothermal reduction of alumina: role of the gaseous alumina phase. *J Eur Ceram Soc* 1993;**12**(2):123–9.
27. Maître A, Lefort P. Solid state reaction of zirconia with carbon. *Solid State Ionics* 1997;**104**(1–2):109–22.